Fundamental x-ray interaction limits in diagnostic imaging detectors: Spatial resolution

G. Hajdok[a)]
Imaging Research Laboratories, Robarts Research Institute, P.O. Box 5015, London, Ontario N6A 5K8, Canada, London Regional Cancer Program, London Health Sciences Centre, London, Ontario N6A 4L6, Canada, and Department of Medical Biophysics, University of Western Ontario, London, Ontario N6A 3K7, Canada

J. J. Battista
Departments of Medical Biophysics and Oncology, University of Western Ontario, London, Ontario N6A 3K7, Canada and London Regional Cancer Program, London Health Sciences Centre, London, Ontario N6A 4L6, Canada

I. A. Cunningham
Imaging Research Laboratories, Robarts Research Institute, P.O. Box 5015, London, Ontario N6A 5K8, Canada, Departments of Diagnostic Radiology and Nuclear Medicine, London Health Sciences Centre, London, Ontario N6A 5W9, Canada, and Department of Medical Biophysics, University of Western Ontario, London, Ontario N6A 3K7, Canada

(Received 6 November 2007; revised 25 March 2008; accepted for publication 19 April 2008; published 19 June 2008)

The practice of diagnostic x-ray imaging has been transformed with the emergence of digital detector technology. Although digital systems offer many practical advantages over conventional film-based systems, their spatial resolution performance can be a limitation. The authors present a Monte Carlo study to determine fundamental resolution limits caused by x-ray interactions in four converter materials: Amorphous silicon (*a*-Si), amorphous selenium, cesium iodide, and lead iodide. The "x-ray interaction" modulation transfer function (MTF) was determined for each material and compared in terms of the 50% MTF spatial frequency and Wagner's effective aperture for incident photon energies between 10 and 150 keV and various converter thicknesses. Several conclusions can be drawn from their Monte Carlo study. (i) In low-*Z* (*a*-Si) converters, reabsorption of Compton scatter x rays limits spatial resolution with a sharp MTF drop at very low spatial frequencies (<0.3 cycles/mm), especially above 60 keV; while in high-*Z* materials, reabsorption of characteristic x rays plays a dominant role, resulting in a mid-frequency ($1-5$ cycles/mm) MTF drop. (ii) Coherent scatter plays a minor role in the x-ray interaction MTF. (iii) The spread of energy due to secondary electron (e.g., photoelectrons) transport is significant only at very high spatial frequencies. (iv) Unlike the spread of optical light in phosphors, the spread of absorbed energy from x-ray interactions does not significantly degrade spatial resolution as converter thickness is increased. (v) The effective aperture results reported here represent fundamental spatial resolution limits of the materials tested and serve as target benchmarks for the design and development of future digital x-ray detectors. [DOI: 10.1118/1.2924219]

Key words: modulation transfer function, diagnostic x-ray detectors, diagnostic x-ray imaging

I. INTRODUCTION

Innovative advances in digital x-ray detector technology have led to a steady transition away from conventional analog-based (e.g., film) image receptors. The motivation for advancing toward a digital approach stems from a continued need to improve image quality, reduce patient dose, increase patient throughput in the imaging clinic, and decrease overall costs. Digital systems potentially address these needs through improved dynamic range and contrast capability, and with separate image acquisition, storage, and display mechanisms.[1]

While detector performance may be limited by a wide variety of factors, conversion and absorption of the incident x-ray energy represents the first and most fundamental step in the x-ray detector chain. The selection of the material in which x rays interact, whether a photoconductor or a phosphor, has a direct impact on the potential performance of the detector.[2] A photoconductor is generally referred to as a direct conversion material because x rays are directly converted to electrical charge with no intermediate energy-conversion stage. In contrast, a phosphor is designated as an indirect conversion material because x rays are first converted to optical light, then finally to electrical charge. The most popular photoconductor and phosphor materials in current practice are amorphous selenium (*a*-Se) and cesium iodide (CsI), respectively.

When designing new x-ray imaging systems, the general performance requirements of the detector depend on the specific imaging task. One important requirement is high-spatial

TABLE I. X-ray fluorescence related constants (Ref. 13) for silicon, selenium, iodine, cesium, and lead.

Quantity	Symbol	Si	Se	I	Cs	Pb
K-fluorescent yield (%)	Y_K	48.5	58.6	88.6	89.8	96.1
Average *L*-fluorescent yield (%)	$\bar{Y}_L$	NA	1.2	7.1	8.1	28.5
K-edge energy (keV)	$(E_B)_K$	1.84	12.66	33.17	35.99	88.01
Average *L*-edge energy (keV)	$(\bar{E}_B)_L$	0.11	1.52	4.87	5.36	14.70
Average *K*-fluorescent energy (keV)	$\bar{h}\nu_K$	1.79	11.86	30.45	32.98	79.94
Average *L*-fluorescent energy (keV)	$\bar{h}\nu_L$	NA	1.40	4.08	4.45	11.58

resolution. Two imaging applications that particularly demand high-spatial resolution include mammography[3] and microcomputed tomography (μ-CT).[4] One of the primary aims in mammography is to perceive the fine details of microcalcifications and thin fibers protruding from a tumor mass in the breast, while in μ-CT, the goal may be to visualize the intricate bony architecture of small animals (e.g., mice). To achieve sufficient spatial resolution in these x-ray imaging applications, a high resolution detector is necessary.

Physical factors that may limit the spatial resolution in a detector include: The size of the detector elements (dels), spatial spread of energy from interacting x-ray quanta, and the spread of secondary image-forming quanta (i.e., electron-hole pairs in photoconductors and optical light in a phosphor). The spread of the incident x-ray energy can play an important role as the energy is not absorbed at the precise location of incidence within a detector material. Rather, x-ray interactions produce secondary radiation (in the form of secondary fluorescent or scatter x rays and secondary charged particles) that spreads the incident x-ray energy away from the primary interaction site.

Several investigations have dealt with the inherent spatial resolution of converter materials used in diagnostic x-ray detectors. Que and Rowlands[5] used analytic equations to describe the main intrinsic factors, including the range of primary photoelectrons and geometric effect due to obliquely incident x rays, which limit spatial resolution in *a*-Se. Boone *et al.*[6] used Monte Carlo simulations to study the effects of x-ray scattering and x-ray fluorescence in a wide variety of converter materials (e.g., *a*-Se, CsI, Gd_2O_2S). In their work, they determined the radial distribution of reabsorbed energy solely from these secondary x rays but did not calculate a corresponding MTF. Furthermore, they ignored energy deposition from secondary electron transport. From these and other investigations,[7] it is known that emission of fluorescent x rays following photoelectric interactions result in a substantial loss in energy absorption at the primary site.

Although x-ray converter materials have been studied and developed for many years, the recent emergence of digital x-ray imaging systems has led to a renewed interest in the performance of both conventional and nonconventional materials. Further investigation into the fundamental limits of these detector materials is necessary to determine if potential improvements can be made, especially in areas that demand high-spatial resolution. In this article, we use Monte Carlo simulations of x-ray photon and electron transport to examine the fundamental limitations imposed by the various x-ray interaction processes on the modulation transfer function (MTF) for direct (amorphous silicon, amorphous selenium, lead iodide) and indirect (cesium iodide) conversion detector materials. For each converter material, the importance of each x-ray interaction process, and their corresponding secondary radiation (i.e., secondary x ray or electron), to MTF degradation is identified and quantified as a function of incident x-ray energy and converter thickness. In addition, selected Monte Carlo results are compared with recently published experimental MTF data to determine if existing detector performance is approaching these fundamental limits. The scope of our study is limited to the spatial distribution of x-ray energy deposition. The subsequent effect of image-forming quanta production and transport within the converter material is not included. Monte Carlo simulation of such effects has been conducted by others[8–10] and is shown to further reduce spatial resolution.

II. BACKGROUND

In the photon energy range of 10–150 keV, the relevant x-ray interaction processes are photoelectric absorption[11] (see Table I for relevant relaxation data), coherent scatter,[12] and Compton scatter.[11,12] Secondary radiation, whether fluorescent/scatter photons or charged particles, from these x-ray interactions can potentially degrade and limit the spatial resolution of a detector material by "blurring" or "spreading" the incident energy away from the primary interaction site. The degree of spread depends on: (i) The x-ray interaction process that leads to the secondary radiation, (ii) the initial launch direction of the secondary radiation, and (iii) the range of the secondary radiation. An elaboration of each dependency is presented in the following sections.

II.A. Energy dependence of x-ray interactions

The relative probability of occurrence for each interaction type is presented in Fig. 1, as a function of photon energy for silicon (Si), selenium (Se), CsI, and lead iodide (PbI_2). As seen from the graph, photoelectric absorption dominates in CsI and PbI_2 over the entire diagnostic energy range (10 −150 keV), but only up to 25 and 60 keV in Si and Se, respectively. At energies below the *K* edges of Se, CsI, and PbI_2, coherent scatter can be significant (5%−10%), while Compton scatter is negligible. Immediately above the *K* edges in these materials, both coherent and Compton scatter

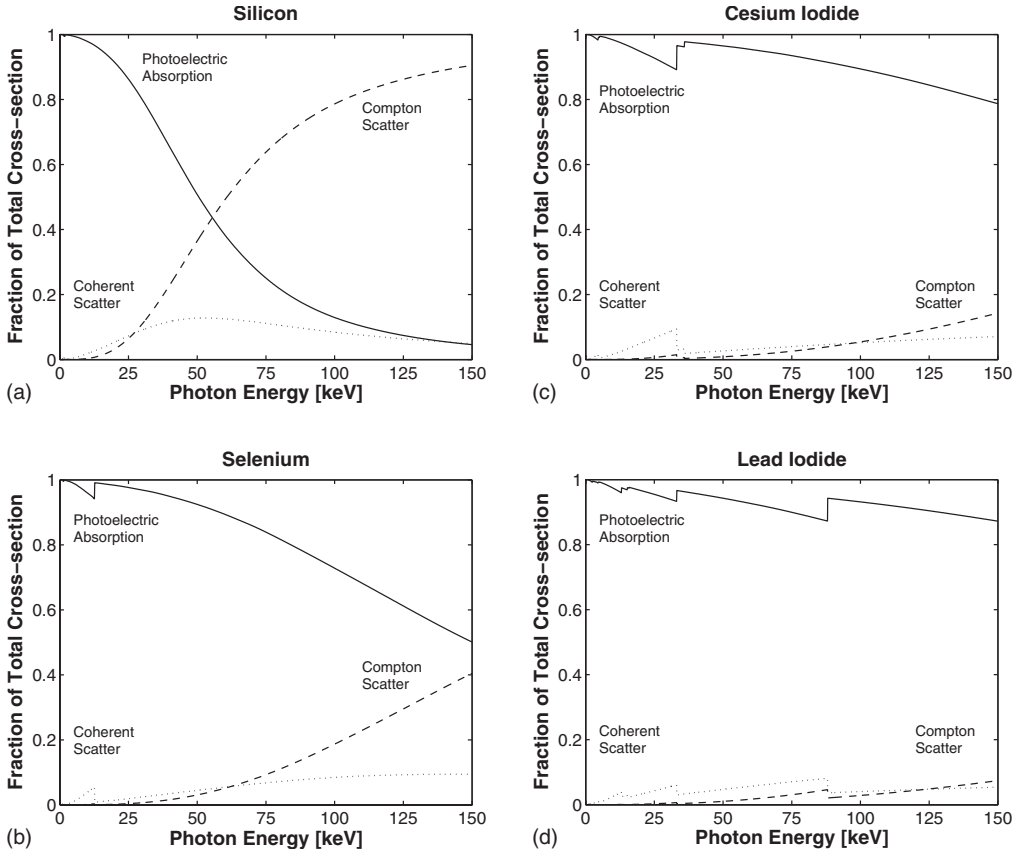

FIG. 1. Relative probability of each x-ray interaction as a function of photon energy for (a) Si, (b) Se, (c) CsI, and (d) PbI_2. The linear cross sections for each x-ray interaction were taken from the XCOM cross-section library (Ref. 14).

events are negligible compared to photoelectric events, but do increase slightly with photon energy thereafter. In contrast, Compton scatter becomes the primary x-ray interaction process above 60 keV in Si, while coherent scatter events vary between 10% and 15% up to 150 keV.

II.B. Angular dependence of secondary radiation

The angular distribution of secondary radiation can be described using the concept of a probability density function (PDF). The normalized probability of scattering a photon or electron into an angle is given by the ratio of the differential cross section per unit angle and the total cross section. The PDFs that describe the directional distribution of secondary radiation from coherent scatter, Compton scatter, and photoelectric events are shown in Fig. 2. In general, these PDFs are complex functions that depend on the energy of the incident x ray and type of material.

In coherent scatter events, the differential cross section per atom is given by the product of the Thomson differential cross section and the square of the atomic form factor F, which relates the scatter amplitude from the collective atomic electron distribution to that from an isolated electron.[15] As seen in Fig. 2(a), the PDF, $\mathrm{pdf}_{\mathrm{coh}}(\theta)$, with respect to the coherent scatter x-ray angle, θ, is given by

$$\mathrm{pdf}_{\mathrm{coh}}(\theta) = \frac{1}{{}_a\sigma_{\mathrm{coh}}} \times \left\{ \frac{r_0^2}{2} \times (1+\cos^2\theta) \times [F(x,Z)]^2 \right\} \times 2\pi \sin\theta, \quad (1)$$

where ${}_a\sigma_{\mathrm{coh}}$ is the total coherent cross section per atom, $r_0 = 2.818 \times 10^{-13}$ cm is the classical electron radius, $x = h\nu/hc \times \sin(\theta/2)$ is the momentum transfer, and Z is the atomic number. In our study, form factors for molecules are calculated based on the independent atom approximation (i.e., form factors of individual atoms combine independently).

As shown in Fig. 2(a), the scattered x ray is emitted predominantly in the forward direction, and even more so as the incident photon energy is increased. In PbI_2, the fraction of coherent scatter x rays emitted laterally between 45° and 135° is 53% at 10 keV and decreases to 15% at 100 keV. Therefore, the lateral emission of coherent scatter x rays may be important at low photon energies for high-atomic number materials.

In Compton scatter events, the differential cross section per electron[16] is given by the product of the Thomson differential cross section and the Klein–Nishina factor F_{KN}, which describes the probability of scatter by an unbound electron. As seen in Fig. 2(b), the PDF, $\mathrm{pdf}_{\mathrm{inc}}(\theta)$, with respect to the Compton scatter x-ray angle, θ, is given by

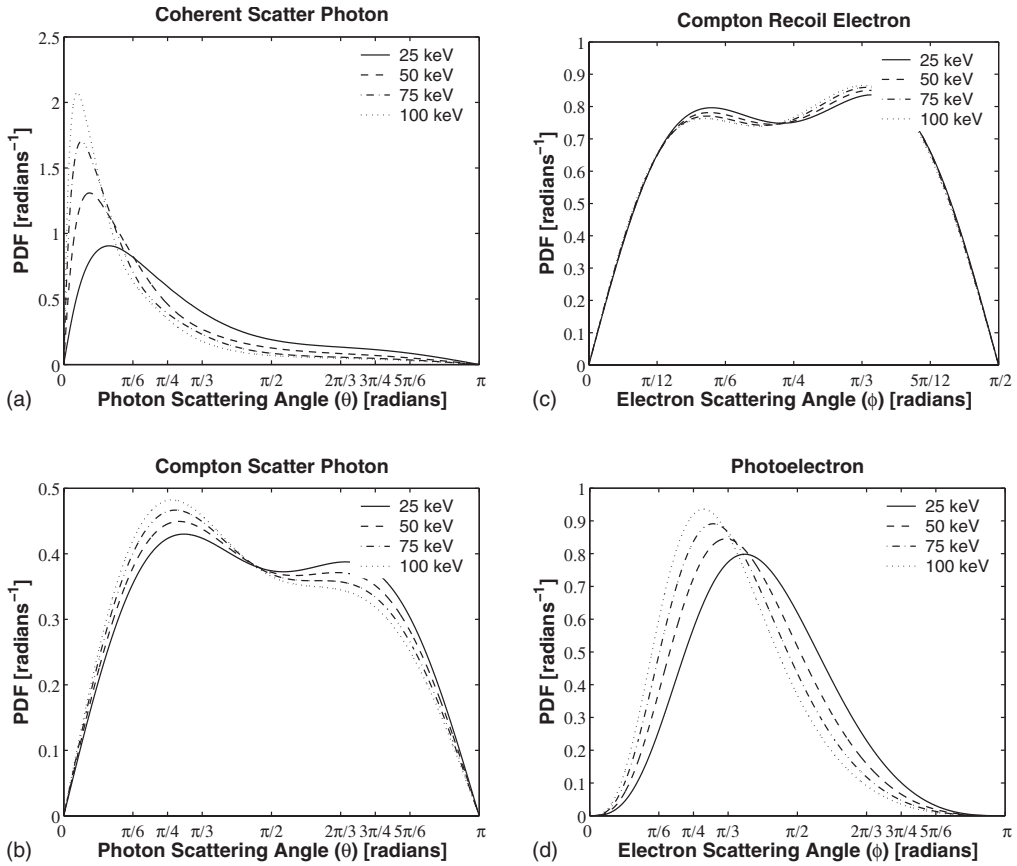

FIG. 2. Angular PDFs for (a) coherent scatter photons (in PbI_2), (b) Compton scatter photons, (c) Compton recoil electrons, and (d) photoelectrons calculated using Eqs. (1), (2), (4), and (6), respectively. Each energy listed in (a), (b), and (c) represent incident photon energies, while those in (d) represent electron kinetic energies.

$$\mathrm{pdf}_{\mathrm{inc}}(\theta)=\frac{1}{{}_e\sigma_{\mathrm{inc}}}\times\left\{\frac{r_0^2}{2}\times(1+\cos^2\theta)\times F_{\mathrm{KN}}(\theta)\right\}\times 2\pi\sin\theta, \tag{2}$$

where ${}_e\sigma_{\mathrm{inc}}$ is the total Compton cross section per electron, r_0 is the classical electron radius, and the Klein–Nishina factor, $F_{\mathrm{KN}}(\theta)$, is given by

$$F_{\mathrm{KN}}(\theta)=\frac{1}{[1+\alpha(1-\cos\theta)]^2}\times\left\{1+\frac{\alpha^2(1-\cos\theta)^2}{(1+\cos^2\theta)[1+\alpha(1-\cos\theta)]}\right\}, \tag{3}$$

where $\alpha=h\nu/m_0c^2$ is the photon energy in units of the electron rest-mass energy.

Similarly, as seen in Fig. 2(c), the PDF, $\mathrm{pdf}_{\mathrm{inc}}(\phi)$, with respect to the Compton recoil electron angle, ϕ, is given by

$$\mathrm{pdf}_{\mathrm{inc}}(\phi)=\frac{1}{{}_e\sigma_{\mathrm{inc}}}\times\left\{\frac{r_0^2}{2}\times(1+\cos^2\theta)\times F_{\mathrm{KN}}(\theta)\right\}\times\frac{-[4(1+\alpha)^2\cos\phi]}{[(1+\alpha)^2-\alpha(2+\alpha)\cos^2\phi]^2}\times 2\pi\sin\phi, \tag{4}$$

where the x-ray scattering angle, θ, and the recoil electron angle, ϕ, are related via

$$\cos\theta=1-\frac{2}{(1+\alpha)^2\tan^2\phi+1}. \tag{5}$$

As shown in Fig. 2(b), the scattered x ray is emitted predominantly in the lateral direction and changes little as the incident photon energy is increased. Consequently, the fraction of Compton scatter x rays emitted laterally between 45° and 135° is approximately constant at 60% in the diagnostic energy range. As shown in Fig. 2(c), the recoil electron is emitted predominantly in a diagonal direction in the same energy range. Due to the atomic number independence of the Compton differential cross section, the lateral and diagonal spread will be identical for all materials.

In photoelectric events, the differential cross section per atom[16,17] is given by the product of the nonrelativistic Fischer differential cross section and the Sauter factor F_{Sauter}, which accounts for the relativistic nature of the photoelectron. As seen in Fig. 2(d), the probability density function, $\mathrm{pdf}_{\mathrm{pe}}(\phi)$, with respect to the photoelectron angle, ϕ, is given by

$$\mathrm{pdf}_{\mathrm{pe}}(\phi)\propto\frac{1}{{}_a\tau}\times\left\{\frac{\sin^2\phi}{(1-\beta\cos\phi)^4}\times F_{\mathrm{Sauter}}(\phi)\right\}\times 2\pi\sin\phi, \tag{6}$$

where ${}_a\tau$ is the total photoelectric cross section per atom, $\beta=v/c$ is the velocity of the electron in units of the speed of light, and the Sauter factor, F_{Sauter}, is given by

$$F_{\text{Sauter}}(\phi)=\beta^2\times\left[\tfrac{1}{2}\gamma^2(1-\beta\cos\phi)-\gamma(1-\beta\cos\phi)+\tfrac{1}{2}(1-\beta\cos\phi)+\gamma^{-1}\right], \quad (7)$$

where $\gamma=(T+m_0c^2)/m_0c^2$ is the ratio of the total electron energy to the electron rest-mass energy.

As shown in Fig. 2(d), photoelectrons are not all emitted in the same direction (i.e., their directional distribution is not isotropic). At low incident x-ray energies (<100 keV), the photoelectrons tend to be ejected at right angles relative to the direction of the incident x ray, and as the energy of the incident x ray is increased (>100 keV), more and more of the photoelectrons are emitted in a forward direction. In contrast, fluorescent x rays and Auger electrons, following a photoelectric event, are emitted isotropically from the atom (not shown in Fig. 2).

II.C. Path-length dependence of secondary radiation

The distance over which secondary radiation transfers the incident photon energy away from the primary interaction site can be analytically estimated from the mean free path (MFP) for photons and the continuous slowing down approximation (CSDA) range (R_{CSDA}) for electrons. The photon MFP represents the average photon interaction distance, which is equal to the reciprocal of the total linear attenuation coefficient μ. The R_{CSDA} represents the average path length of an electron of a given kinetic energy as it slows down in a medium. Note that R_{CSDA} is larger than but linearly related to the average depth of penetration (projected range). Based on experimental data,[11] the maximum projected range is approximately 90% of R_{CSDA} in low Z materials (e.g., Si); while for high Z materials, their ratio decreases to 50%. The MFP and R_{CSDA} are plotted in Fig. 3. Of the materials shown, PbI_2 has the smallest photon MFP due to the (cubed) atomic number dependence of photoelectric interactions, while all materials have approximately the same electron range because of their similar density. Photons generally transport energy approximately two orders of magnitude farther than electrons. However, electrons are responsible for depositing the primary energy of the incident photon, and the spread of energy will become important when quantifying spatial resolution.

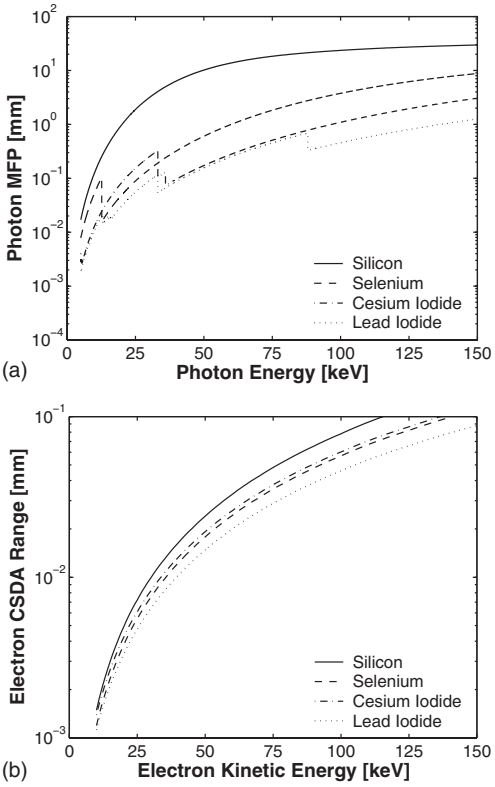

FIG. 3. (a) Photon mean free paths as a function of photon energy and (b) electron CSDA ranges as a function of electron kinetic energy for Si, Se, CsI, and PbI_2. Linear attenuation coefficients were taken from the XAAMDI database (Ref. 18) and CSDA ranges were taken from the ESTAR database (Ref. 19).

III. METHODS

III.A. Monte Carlo code

The latest version of the Electron Gamma Shower (EGSnrc) Monte Carlo code[20,21] was used to simulate the coupled photon-electron transport within typical x-ray converter materials. The user code DOSRZnrc (Ref. 22) was used to determine the spatial distribution of dose (i.e., absorbed energy per unit mass) within a cylindrical slab geometry.

Some of the relevant new features of EGSnrc include: (i) PRESTA-II electron transport algorithm, (ii) bound Compton scattering, (iii) photoelectron angular sampling, and (iv) atomic relaxation by release of fluorescent photons (K,L,M shells), and Auger or Coster–Kronig electrons.

The EGSnrc Monte Carlo code has a number of parameters that control the transport of particles. The parameters PCUT and ECUT, which represent the minimum total energy (kinetic plus rest mass) below which no radiation transport takes place, were set to 1 and 512 keV for photons and electrons, respectively. The general rule of thumb for calculating dose distributions requires that ECUT be chosen so that the electron range at ECUT is less than 1/3 of the smallest dimension in the dose scoring region.[23,24] Based on the above value of ECUT, the corresponding electron range satisfied the latter criterion for all materials used in our simulations. To distinguish between the effects from secondary x rays and electrons, simulations were also performed with the value of ECUT set to the incident photon energy thereby suppressing electron transport (i.e., "on-the-spot" energy deposition). One other feature taken advantage of was the ability to include or exclude the simulation of coherent scatter events.

III.B. Detector geometry

The modeled detector geometry, shown schematically in Fig. 4, consisted of an infinitesimal pencil beam of x-ray

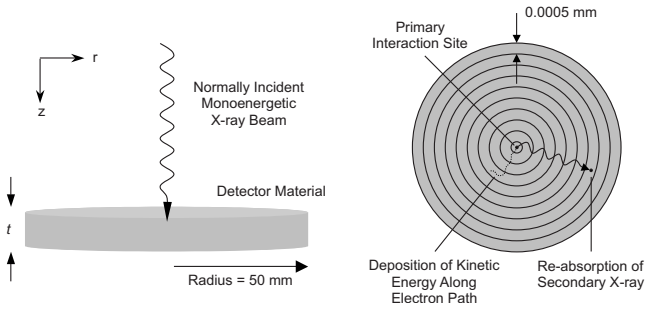

FIG. 4. Detector geometry in cylindrical coordinates (r,z) modeled in the Monte Carlo simulations. The thickness t for each converter material was calculated [see Eq. (8)] for several quantum efficiency values, ranging between 0.10 and 0.99, at each incident photon energy.

photons incident perpendicularly on the center of a uniform cylindrical slab (10 cm diameter) of x-ray converter material. Each slab was subdivided into 100 000 concentric annuli with an equal spacing of 0.5 μm each. Four types of x-ray converter materials, which span a wide range of atomic numbers, were modeled in our study: (i) amorphous silicon (a-Si), (ii) a-Se, (iii) CsI, and (iv) PbI_2. The appropriate density of each converter was chosen to agree with those used in practice. The thickness, t, of each material was based on a specific quantum efficiency value, η, at a given incident photon energy, as given by

$$t_\eta(h\nu,Z) = -\frac{\ln(1-\eta)}{\mu(h\nu,Z)}, \tag{8}$$

where μ is the linear attenuation coefficient at photon energy, $h\nu$, and atomic number, Z. Various quantum efficiency values ranging from 0.10 to 0.99 (0.10 intervals) were examined for each incident photon energy. Note that since spatial resolution generally degrades with increasing converter thickness, then the 0.99 quantum efficiency thickness is considered to represent the lower limit or worst-possible resolution.

III.C. Spatial distribution of absorbed energy

Monte Carlo simulations were used to generate dose deposition profiles $d(r)$, which represent the radial distribution of absorbed energy per unit mass within the converter material. These profiles form the basis of the one-dimensional radial point spread function (PSF) $p(r)$, when normalized to unit area

$$p(r) = \frac{d(r)}{2\pi\int d(r) r\,\mathrm{d}r}. \tag{9}$$

Dose deposition profiles were determined for each x-ray converter material at monoenergetic x-ray energies, ranging from 10 to 150 keV, in 1 keV intervals, which represent the different energies encountered in diagnostic x-ray spectra. One million incident x-ray histories were used in each Monte Carlo run, which was sufficient to reduce the statistical uncertainty in the dose deposition profiles to negligible levels.

III.D. X-ray interaction modulation transfer function

Based on $p(r)$, the x-ray interaction MTF, $\mathrm{MTF}_x(k)$, was calculated using the Hankel transform via

$$\mathrm{MTF}_x(k) = \mathcal{H}\{p(r)\} = 2\pi\int_0^\infty p(r)J_0(2\pi kr)r\,\mathrm{d}r, \tag{10}$$

where k corresponds to a radial spatial frequency, $\mathcal{H}$ is the Hankel transform operator, and J_0 is the zero-order Bessel function. Equation (10) represents the spatial-frequency variation of spatial resolution from the spread of absorbed energy due to x-ray interactions.

III.E. Figures of merit

To characterize the energy and thickness dependence of the spatial resolution of each converter material, we chose to use both the 50% MTF frequency, f_{50}, and the effective sampling aperture, a_e.[25,26]

The a_e is the reciprocal of the volume under the squared MTF, and for the case of a circularly symmetric MTF is given by

$$a_e = \left[2\pi\int_0^\infty \mathrm{MTF}^2(k)k\,\mathrm{d}k\right]^{-1}. \tag{11}$$

Thus, the greater the volume under the squared MTF, the smaller the a_e, and vice versa. The a_e has units of area, but it can also be stated as the diameter of the equivalent circle with the same area. In accordance with the work of Wagner,[25,26] we have adopted the latter in this article. Note that the a_e used in our study physically represents the average blur size caused by the spread of absorbed energy from x-ray interactions in a converter material.

Since the MTF cannot be determined to infinite frequency in practice, we have chosen to integrate the a_e up to the spatial frequency where the MTF falls to 2%, which is high enough to ensure an accurate integral while minimizing noise contributions at high spatial frequency. Based on an annuli spacing of 0.5 μm, the corresponding Nyquist frequency in our Monte Carlo simulations is 1000 cycles/mm. Accurate behavior of the MTF up to such a high spatial frequency is an important necessity since the short-range nature of electrons will affect how the MTF will behave in that region. A Monte Carlo code with accurate electron transport, which EGSnrc provides, is thus required to obtain reasonable values for the a_e.

III.F. Comparison with published experimental data

Considerable experimental research on the detector performance of a-Si,[27,28] a-Se,[29–32] CsI,[33–37] and PbI_2 (Refs. 38–41) has been reported in the literature. The fundamental spatial resolution limits of these detectors were assessed by

TABLE II. X-ray beam and detector parameters used in the prototype systems.

Converter material	X-ray beam quality (kVp)	X-ray beam filtration (mm)	Detector thickness (μm)	Detector element size (μm)	Nyquist frequency (cycles/mm)
a-Si [a]	26	0.4	1000	50	10.00
a-Se [b]	70	2.0	300	134	3.73
CsI[c]	80	20.0	350	200	2.50
PbI_2 [d]	70	2.0	100	100	5.00

[a]Reference 28.
[b]Reference 30.
[c]Reference 34.
[d]Reference 40.

comparing MTFs from our Monte Carlo simulations and published experimental measurements. Additional Monte Carlo simulations were needed to match the imaging parameters listed in Table II. In these simulations, the incident x-ray spectra were modeled using an in-house MATLAB (Mathworks, Natick, MA) code based on the semiempirical Tucker–Barnes[42] diagnostic x-ray spectral model.

The experimental MTFs reported in the literature represent presampled system MTF values, while the x-ray interaction MTFs from the Monte Carlo simulations represent only the contribution from the spread of the incident x-ray energy. To allow for a direct comparison with experimental results, the x-ray interaction MTF, $\mathrm{MTF}_x(k)$, was adjusted to account for the finite detector element (del) size, a_{del}, of the prototype detector systems. The Monte Carlo presampling MTF, $\mathrm{MTF}_{\mathrm{pre}}(k)$, was obtained by including this aperture effect using

$$\mathrm{MTF}_{\mathrm{pre}}(k) = \mathrm{MTF}_x(k) \times \left|\mathrm{sinc}(\pi a_{\mathrm{del}} k)\right|. \quad (12)$$

IV. RESULTS

IV.A. X-ray interaction MTF

Figure 5 shows x-ray interaction MTFs for each converter material tested at selected incident monoenergetic photon energies between 10 and 100 keV. To distinguish between the effects of secondary x rays and electrons, results are shown with electron transport enabled in column I and disabled in column II. In general, these results show that: (i) secondary x rays (fluorescent and scatter x rays) cause a sharp low-frequency drop in the MTF within the range of 0 −3 cycles/mm; and (ii) secondary electrons (photoelectrons and Compton recoil electrons) cause an additional drop in the MTF with increasing frequency above approximately 10−15 cycles/mm.

In *a*-Si, a substantial MTF drop below 1 cycle/mm is observed which increases in magnitude with increasing photon energy. The reabsorption of Compton scatter x rays is primarily responsible for the drop with the fractional amount approximately equal to the relative probability of Compton scatter events (15% at 30 keV and 55% at 70 keV). The severity of the drop is due to the fact that Compton scatter x rays retain a significant fraction of the incident energy (>80% on average within the diagnostic energy range) and have a high probability of being emitted laterally [see Fig. 2(b)]. Although photoelectric absorption is the dominant x-ray interaction process below 60 keV, the energy of the resulting *K* fluorescent x ray is too low (~1 keV) to have significant impact. The effect of photoelectron and Compton recoil electron transport is minor since the former becomes less prevalent with increasing incident energy, while the latter only receives a small fraction of the incident energy.

In *a*-Se, the MTF demonstrates good resolution up to 50 cycles/mm for incident energies below 50 keV, where there is a gradual drop (20%) due to reabsorption of *K* fluorescent x rays. At 100 keV, a sharp low-frequency MTF drop occurs due to reabsorption of Compton scatter x rays. Also, photoelectrons have a high kinetic energy (87 keV for an incident photon energy of 100 keV), and as a result, cause a substantial drop at approximately 15 cycles/mm and above.

In CsI, the MTF exhibits good resolution below 33 keV (*K* edge of iodine). At 36 keV (*K* edge of cesium) reabsorption of *K* fluorescent x rays cause a significant low-frequency drop (40% by 5 cycles/mm). As the incident photon energy increases, the magnitude of the drop decreases (20% at 100 keV). Similar to *a*-Se, at 100 keV, there is a substantial MTF drop above 15 cycles/mm due to the transport of photoelectrons.

Similar to CsI, the MTF for PbI_2 shows good spatial resolution below 33 keV. Between 34 and 87 keV, a 20% drop occurs near 5 cycles/mm from the reabsorption of *K* fluorescent x rays in iodine. Above the *K* edge of Pb (88 keV), the MTF drop becomes more severe (40% at 2 cycles/mm) because of *K* fluorescent x rays from lead. The spread of photoelectrons is small, due to the high stopping power of Pb, and thus the effect on the MTF is minor.

IV.B. Dependence on incident x-ray energy

The spatial resolution performance of each converter material is plotted in Fig. 6 as a function of incident photon energy. Performance here is quantified in terms of both the

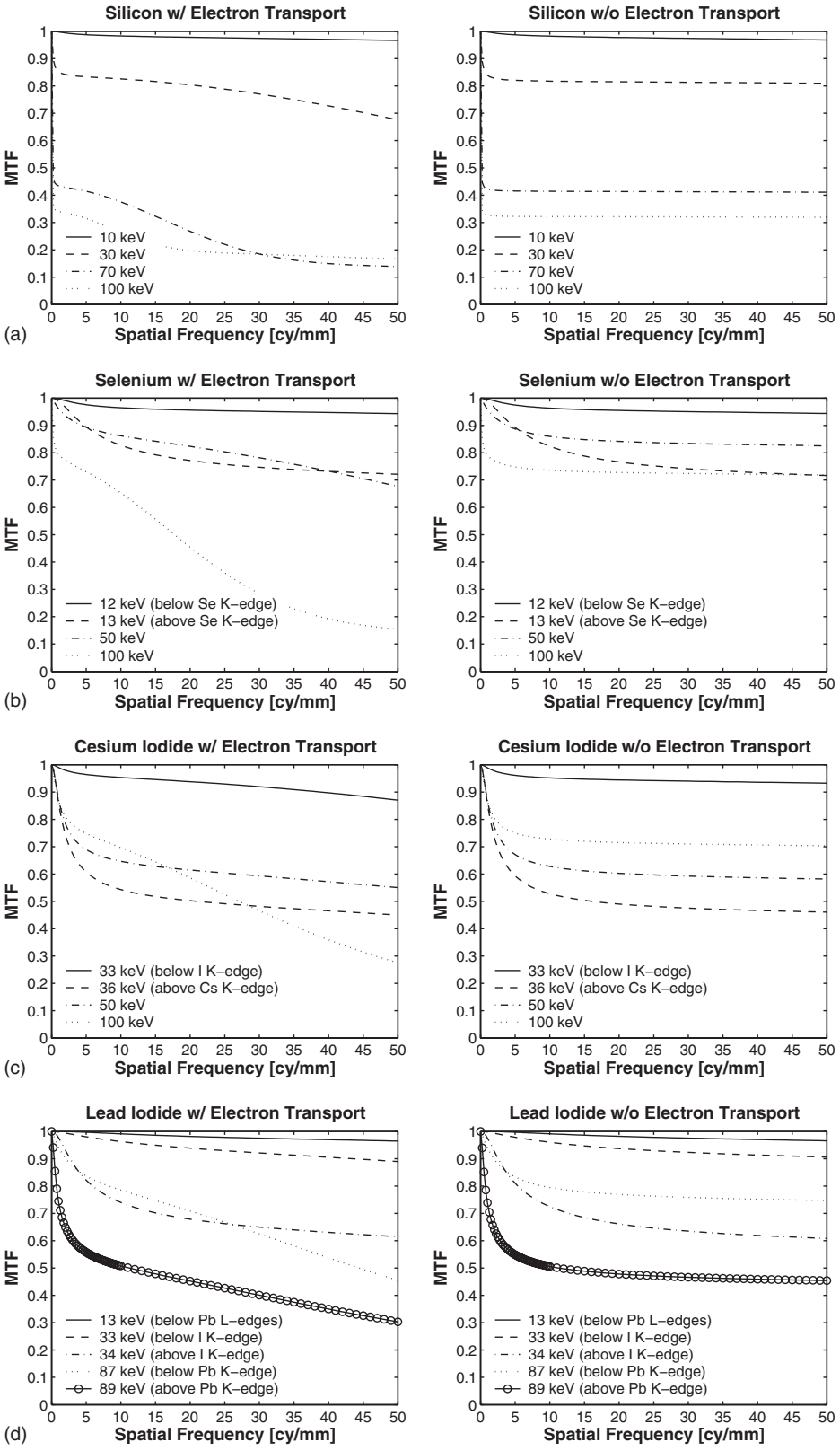

FIG. 5. Monte Carlo x-ray interaction MTFs for each converter material at selected incident monoenergetic photon energies below 100 keV. Results are presented with electron transport enabled (column I) and disabled (column II).

50% MTF frequency (column I) and effective aperture (column II). To isolate the effects of coherent scatter, each figure displays two separate profiles corresponding to Monte Carlo simulations that include all x-ray interactions and those with coherent scatter events disabled.

In the case of the 50% MTF spatial frequency, its trend generally decreases with increasing incident energy. At low energies (20 keV), f_{50} values are extremely high (300 $-$500 cycles/mm) for all materials; while at high energies (150 keV), f_{50} values vary between 6 and 15 cycles/mm for

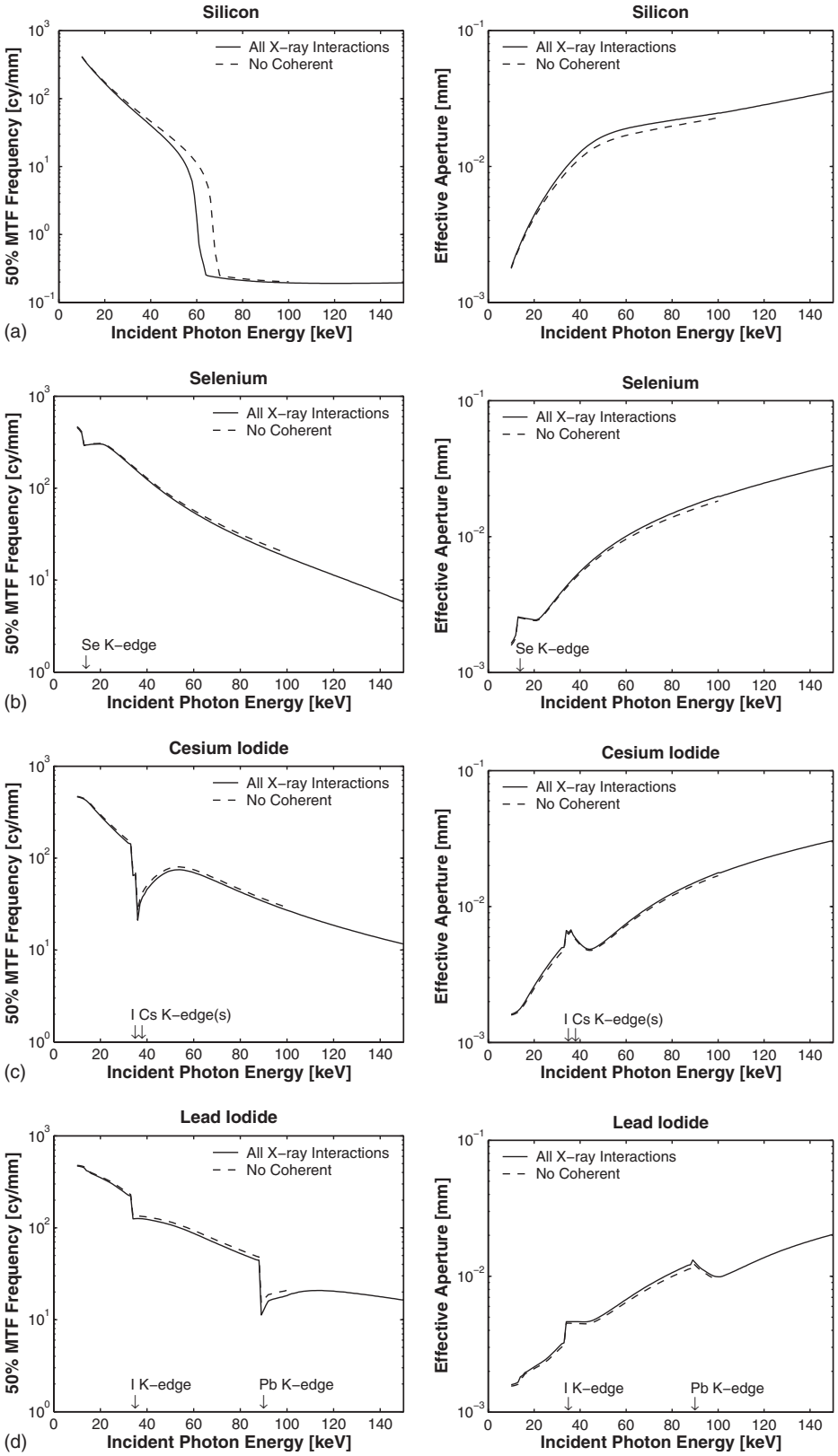

FIG. 6. Spatial resolution performance, expressed in terms of the 50% MTF spatial frequency (column I) and effective aperture (column II), as a function of incident photon energy for each converter material. Results are shown for Monte Carlo simulations with all x-ray interactions and without coherent scatter events included.

all materials except *a*-Si. In *a*-Si, f_{50} values drop sharply to 0.2 cycles/mm at 60 keV due to Compton scatter becoming the dominant x-ray interaction process. In the other materials, there are abrupt drops in f_{50} values at their respective *K*-edge energies. In *a*-Se, the drop is negligible, while in CsI, f_{50} values fall to 20 cycles/mm (Cs and I *K* edges), and to 10 cycles/mm in PbI_2 (Pb *K* edge). The influence of coherent scatter is only important in *a*-Si within a narrow window between 60 and 70 keV, where coherent scatter events make up approximately 15% of all x-ray interactions.

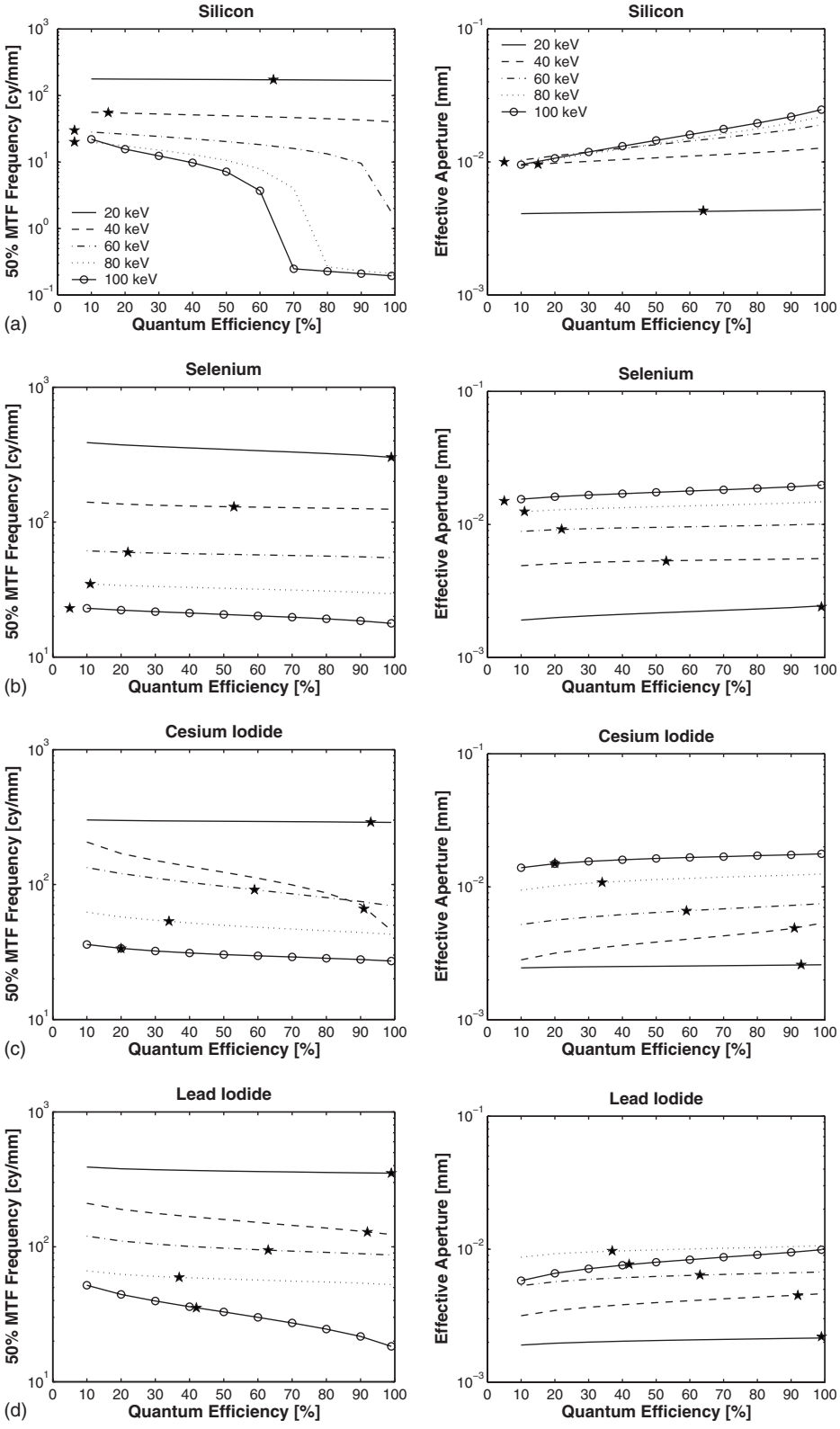

FIG. 7. Spatial resolution, expressed in terms of f_{50} (column I) and a_e (column II), as a function of thickness for each converter material at selected incident photon energies. Converter thickness is defined in terms of a quantum efficiency value ranging between 0.10 and 0.99 [see Eq. (8)]. At each energy, points indicated with a star (⋆) represent a typical thickness (1 mm for *a*-Si; 250 μm for all others) used in practice.

In contrast, in terms of the effective aperture, the trend for each converter material is similar and progressively increases with increasing incident energy. At low energies (20 keV), the a_e values are approximately $2-3$ μm, while at high energies (150 keV), the values begin to level out at around $20-35$ μm. The effect of coherent scatter x rays is negligible for each material.

IV.C. Dependence on x-ray converter thickness

In general, spatial resolution degrades with increasing detector thickness. However, as shown in Fig. 7, the x-ray interaction MTF has only a minor dependence on thickness in most cases. The effect on both f_{50} and a_e is shown as a function of thickness for each converter material at selected

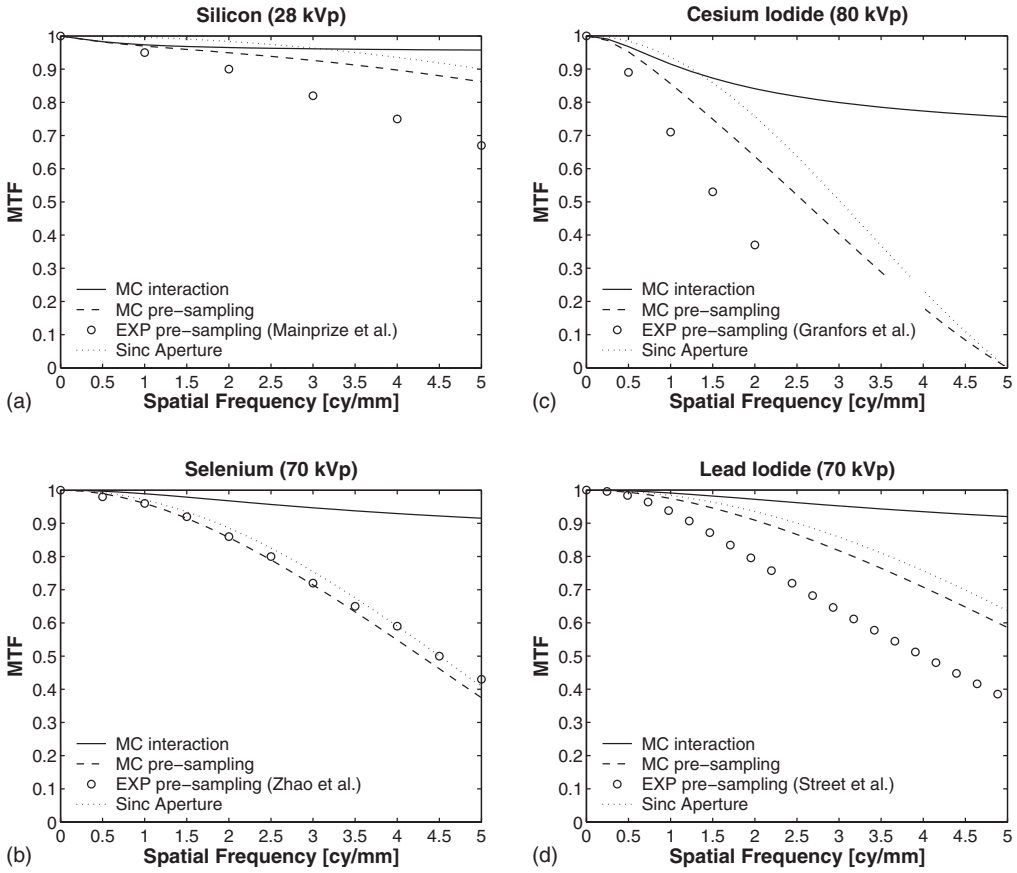

FIG. 8. Comparison of Monte Carlo (MC) and experimental (EXP) presampling MTFs for each converter material. References and x-ray beam and detector parameters are given in Table II.

incident photon energies below 100 keV. Converter thickness is expressed here as a quantum efficiency value ranging between 0.10 and 0.99. To provide a context for these results, each graph also shows results for a typical converter thickness used in practice (1 mm for *a*-Si; 250 μm for all others).

In all cases except *a*-Si, photoelectric events dominate and there is very little thickness dependence when the incident x-ray energy is below the applicable *K* edge energy. At energies approximately 20 keV (or more) greater than the *K*-edge energies, photoelectrons receive a significant fraction of the incident energy. Since the photoelectron range is always much less than the detector thickness, there is little thickness dependence. Only at energies just above the *K*-edge energies, where *K* fluorescent x-ray reabsorption plays a significant role, is there a significant depth dependence. Averaged over a typical diagnostic spectrum of x-ray energies, the depth dependence is minor.

In *a*-Si, the depth dependence is more complex. For example, below approximately 60 keV, photoelectric events dominate and there is very little depth dependence as all incident x rays have an energy much greater than the *K*-edge energy. Above 60 keV, Compton interactions dominate and the f_{50} value drops rapidly with increasing thickness. This depth dependence increases with increasing incident x-ray energy.

IV.D. Comparison with published experimental data

The importance of x-ray interaction spread in existing diagnostic x-ray detectors is demonstrated in Fig. 8, where the Monte Carlo x-ray interaction MTF is compared to published presampling MTF measurements for selected *a*-Si, *a*-Se, CsI, and PbI_2 detectors. In each plot, the x-ray interaction MTF is also scaled by a sinc function appropriate for the stated detector element size to give the Monte Carlo presampling MTF. Comparison of the Monte Carlo and experimental presampling MTF curves give an indication of which blurring mechanism ultimately limits spatial resolution. Each material shown represents a flat-panel detector used either for mammography (*a*-Si) or radiography (*a*-Se, CsI, PbI_2).

The measured presampling MTFs implicitly include other sources of signal spreading that are not included in our Monte Carlo simulations, such as charge diffusion in photoconductors and optical light spread in phosphors. As expected, good agreement occurs with *a*-Se, suggesting that detector element size is the primary factor limiting resolution.[30] Results for the other detectors show that other physical processes are more important than detector element size and x-ray interaction spread in determining spatial resolution.

TABLE III. Spatial resolution performance comparison of the x-ray converter materials examined in our study under mammography and μ-CT conditions. Both resolution indices are included: 50% MTF spatial-frequency (f_{50}) and effective aperture (a_e). Also noted is the type of secondary radiation limiting the resolution in each converter material.

	Mammography (20 keV)		μ-CT (40 keV)		
Converter material	f_{50} (cycles/mm)	a_e (mm)	f_{50} (cycles/mm)	a_e (mm)	Primary source of degradation
a-Si	168	0.004	40	0.013	Compton scatter x rays
a-Se	302	0.002	125	0.006	K fluorescent x rays
CsI	288	0.003	46	0.005	L (<33 keV) and K (>33 keV) fluorescent x rays
PbI_2	351	0.002	123	0.005	L (<33 keV) and K (>33 keV) fluorescent x rays

V. DISCUSSION

The results of our Monte Carlo study represent upper limits of spatial resolution performance for x-ray detectors used in diagnostic imaging. Table III summarizes results as they might apply to two high-resolution imaging applications, mammography and μ-CT, and also lists the primary cause(s) of resolution degradation. At mammography energies, each material possesses high f_{50} (>100 cycles/mm) and low a_e (2–4 μm) values, superior to any existing digital or film-screen system at present. For μ-CT, a-Se and PbI_2 have significantly higher f_{50} values (~125 cycles/mm) compared to a-Si and CsI (~40 cycles/mm), while a-Si has twice the a_e (~12 μm) of the other materials (~5 μm). The limiting detector resolution in current μ-CT systems (excluding geometric magnification) is approximately 25 μm. Overall, these results suggest that spatial resolution performance in mammography and μ-CT are far from fundamental limits imposed by x-ray interactions.

The effective aperture is a useful concept within the context of our study because it can be used to infer the minimum detector element size below which no further improvement in resolution can be achieved. In low-energy applications, such as mammography and μ-CT, a_e is 2–10 μm, while in higher energy applications, such as radiography and clinical CT, the a_e is 10–20 μm. In comparison, current detector element sizes of flat-panel detectors used in mammography and radiography are approximately 50 and 200 μm, respectively. Clearly, these values are much greater than the fundamental x-ray interaction limits.

The loss in spatial resolution due to the spread of the absorbed x-ray energy had an unexpected small dependence on converter thickness. Although such a statement may imply an opportunity to improve quantum efficiency (by increasing converter thickness) without sacrificing resolution (e.g., a-Si at 50 keV), care should be taken not to misinterpret our results. In practice, two important effects, diffusion of secondary image-forming quanta and obliquely incident x rays, cause a trade-off between converter thickness and resolution. In the former case, it has been shown in phosphor-based x-ray detectors that optical light transport significantly degrades the MTF as converter thickness increases.[43–45] In the latter case, x-ray beam divergence results in a range of incident angles (depending on imaging geometry), which not only reduces resolution as these angles becomes more oblique,[46,47] but also results in asymmetric point response functions.[48,49] Therefore, the results presented here cannot be used alone to predict an optimal thickness of practical x-ray detectors for diagnostic imaging.

The results of our Monte Carlo study provide quantifiable spatial resolution benchmarks for imaging scientists/manufacturers to strive for when assessing not only current x-ray detector systems, but also in the development of future designs. An important question remains: "Can these target benchmarks be achieved given the current limitations imposed by secondary image-forming quanta transport?" Recent advances in detector fabrication technology suggest that these benchmarks may potentially be achievable goals. In the case of indirect detection active matrix flat-panel imagers (AMFPI), microelectromechanical-based fabrication techniques have been used to design a segmented phosphor based electronic portal imaging device,[50–52] which consists of a two-dimensional matrix of optically isolated cells dimensionally matched to the pixels of the underlying AMFPI array. Such a design would enable the use of a thick phosphor layer without the accompanying loss in spatial resolution due to optical light diffusion. In principle, this concept could be adapted to diagnostic x-ray detectors as microfabrication techniques continue to be refined.

It should be emphasized that x-ray detectors for high-resolution imaging applications require good signal and noise performance at high-spatial frequencies, as characterized by the detective quantum efficiency (DQE). For example, correlated noise from x-ray interactions can be beneficial in order to partially preserve the DQE in the presence of MTF losses.[53] However, uncorrelated noise may result in a DQE that is proportional to the squared MTF. To be successful, a detector must have both a good MTF and DQE. Noise from x-ray interactions is addressed in the following companion article.[54]

VI. CONCLUSIONS

Monte Carlo simulations were used to determine the spatial distribution of absorbed x-ray energy (per unit mass), giving the point spread function for various x-ray converter materials (a-Si, a-Se, CsI, PbI_2) as a function of incident photon energy and converter thickness. The "x-ray interaction" MTF was determined from each PSF and used to characterize the energy and thickness dependence of the 50%

MTF frequency and Wagner's effective aperture. In low-Z materials (a-Si), reabsorption of Compton scatter x rays substantially degrades resolution above 60 keV, while in higher-Z materials (a-Se, CsI, PbI_2), reabsorption of K fluorescent x rays has a significant effect immediately above their K edges. The effect of secondary electron transport is only significant in a-Se and CsI above 100 keV. In contrast to the spread of optical light in phosphor-based detectors, converter thickness has a minor effect on the spread of the absorbed x-ray energy, and hence, does not significantly influence the trade-off between quantum efficiency and spatial resolution. The effective aperture based on represents the smallest useful digital detector element size. In mammography and μ-CT, a_e values range from 2–4 and 5–13 μm, respectively.

In terms of spatial resolution performance within the diagnostic energy range, it is concluded that all converter materials will work well for mammography and μ-CT applications, while a-Si suffers a significant resolution loss at energies above 60 keV.

ACKNOWLEDGMENTS

The authors are grateful for financial support from the Canadian Institutes of Health Research (CIHR) and Ontario Research and Development Challenge Fund (ORDCF/OCEBCRI project).

[a]Author to whom correspondence should be addressed. Present address: Imaging Research Labs, Robarts Research Institute, P.O. Box 5015, 100 Perth Drive, London, Ontario N6A 5K8, Canada. Telephone: (519) 685-8300 ext 34035; Fax: (519) 663-3900. Electronic mail: ghajdok@imaging.robarts.ca

[1]M. J. Yaffe and J. A. Rowlands, "X-ray detectors for digital radiography," Phys. Med. Biol. **42**, 1–39 (1997).
[2]J. A. Rowlands and J. Yorkston, "Flat panel detectors for digital radiography," in *Handbook of Medical Imaging, Vol. 1. Physics and Psychophysics*, edited by J. Beutel, H. L. Kundel, and R. L. Van Metter (SPIE, Bellingham, WA, 2000), pp. 223–328.
[3]M. J. Yaffe, "Digital mammography," in *Handbook of Medical Imaging, Vol. 1. Physics and Psychophysics*, edited by J. Beutel, H. L. Kundel, and R. L. Van Metter (SPIE, Bellingham, WA, 2000), pp. 329–372.
[4]D. W. Holdsworth and M. M. Thornton, "Micro-CT in small animal and specimen imaging," Trends Biotechnol. **20**, S34–S39 (2002).
[5]W. Que and J. A. Rowlands, "X-ray imaging using amorphous selenium: Inherent spatial resolution," Med. Phys. **22**, 365–374 (1995).
[6]J. M. Boone, J. A. Siebert, J. M. Sabol, and M. Tecotzky, "A Monte Carlo study of x-ray fluorescence in x-ray detectors," Med. Phys. **26**, 905–916 (1999).
[7]B. A. Arnold and B. E. Bjarngard, "The effect of phosphor K x-rays on the MTF of rare-earth screens," Med. Phys. **6**, 500–503 (1979).
[8]A. Badano and M. J. Flynn, "Monte Carlo modelling of the luminance spread function in flat panel displays," Proc. Int. Display Res. Conf. **21**, 382–385 (1997).
[9]A. Badano, "Image quality degradation by light scattering processes in high performance display devices for medical imaging," Ph.D. thesis, University of Michigan, 1999.
[10]A. Badano and J. Sempau, "MANTIS: Combined x-ray, electron, and optical Monte Carlo simulations of indirect imaging systems," Phys. Med. Biol. **51**, 1545–1561 (2006).
[11]F. H. Attix, *Introduction to Radiological Physics and Radiation Dosimetry* (Wiley, New York, 1986).
[12]H. E. Johns and J. R. Cunningham, *The Physics of Radiology*, 4th ed. (Charles C. Thomas, Springfield, IL, 1983).
[13]S. T. Perkins, D. E. Cullen, M. H. Chen, J. H. Hubbell, J. A. Rathkopt, and J. H. Scofield, "Tables and graphs of atomic subshell and relaxation data derived from the LLNL evaluated atomic data library (EADL) for $Z=1-100$," *Technical Report UCRL–50400* (Lawrence Livermore National Laboratory, Livermore, CA, 1991).
[14]M. J. Berger, J. H. Hubbell, and S. M. Seltzer, "XCOM: Photon cross sections database," *Technical Report NBSIR 87–3597* (National Institute of Standards and Technology, Gaithersburg, MD, 1999).
[15]J. H. Hubbell and I. Overbo, "Relativistic atomic form factors and photon coherent scattering cross sections," J. Phys. Chem. Ref. Data **8**, 69–105 (1979).
[16]C. M. Davisson and R. D. Evans, "Gamma-ray absorption coefficients," Rev. Mod. Phys. **24**, 79–107 (1952).
[17]R. D. Evans, *The Atomic Nucleus* (McGraw-Hill, New York, 1955).
[18]J. H. Hubbell and S. M. Seltzer, "Tables of x-ray mass attenuation coefficients and mass energy-absorption coefficients," *Technical Report NISTIR 5632* (National Institute of Standards and Technology, Gaithersburg, MD, 1999).
[19]M. J. Berger, J. S. Coursey, and M. A. Zucker, "ESTAR: Stopping-power and range tables for electrons," *Technical Report NISTIR 4999* (National Institute of Standards and Technology, Gaithersburg, MD, 2000).
[20]I. Kawrakow and D. W. O. Rogers, "The EGSnrc code system: Monte Carlo simulation of electron and photon transport," *Technical Report PIRS-701* (National Research Council of Canada, Ottawa, Ontario, 2000).
[21]I. Kawrakow, "Accurate condensed history Monte Carlo simulation of electron transport. I: EGSnrc, the new EGS4 version," Med. Phys. **27**, 485–498 (2000).
[22]D. W. O. Rogers, I. Kawrakow, J. P. Seuntjens, B. R. B. Walters, and E. Mainegra-Hing, "NRC user codes for EGSnrc," *Technical Report PIRS-702* (National Research Council of Canada, Ottawa, Ontario, 2003).
[23]D. W. O. Rogers, "Low energy electron transport with EGS," Nucl. Instrum. Methods **227**, 535–548 (1984).
[24]A. F. Bielajew and D. W. O. Rogers, in *Monte Carlo Transport of Electrons and Photons*, edited by T. M. Jenkins, W. R. Nelson, A. Rindi, A. E. Nahum, and D. W. O. Rogers (Plenum, New York, 1988), pp. 115–137.
[25]R. F. Wagner, K. E. Weaver, E. W. Denny, and R. G. Bostrom, "Towards a unified view of radiological imaging systems. Part I: Noiseless images," Med. Phys. **1**, 11–24 (1974).
[26]R. F. Wagner, "Towards a unified view of radiological imaging systems. Part II: Noisy images," Med. Phys. **4**, 279–296 (1977).
[27]J. G. Mainprize, N. L. Ford, S. Yin, T. Tumer, and M. J. Yaffe, "Image quality of a prototype direct conversion detector for digital mammography," Proc. SPIE **3659**, 398–406 (1999).
[28]J. G. Mainprize, N. L. Ford, S. Yin, T. Tumer, and M. J. Yaffe, "A slot-scanned photodiode-array/CCD hybrid detector for digital mammography," Med. Phys. **29**, 214–225 (2002).
[29]W. Zhao, W. G. Ji, J. A. Rowlands, and A. Debrie, "Investigation of imaging performance of amorphous selenium flat-panel detectors for digital mammography," Proc. SPIE **4320**, 536–546 (2001).
[30]W. Zhao, I. Blevis, S. Germann, J. A. Rowlands, D. Waechter, and Z. Huang, "Digital radiology using active matrix readout of amorphous selenium: Construction and evaluation of a prototype real-time detector," Med. Phys. **24**, 1834–1843 (1997).
[31]W. Zhao, W. G. Ji, A. Debrie, and J. A. Rowlands, "Imaging performance of amorphous selenium based flat-panel detectors for digital mammography: Characterization of a small area prototype detector," Med. Phys. **30**, 254–263 (2003).
[32]A. L. Goertzen, V. Nagarkar, R. A. Street, M. J. Paulus, J. M. Boone, and S. R. Cherry, "A comparison of x-ray detectors for mouse ct imaging," Phys. Med. Biol. **49**, 5251–5265 (2004).
[33]S. Vedantham, A. Karellas, S. Suryanarayanan, D. Albagli, S. Han, J. E. Tkaczyk, C. E. Landberg, P. R. Granfors, I. Levis, C. J. D'Orsay, and R. E. Hendricks, "Full breast digital mammography with an amorphous silicon based flat panel detector: Physical characteristics of a clinical prototype," Med. Phys. **27**, 558–567 (2000).
[34]P. R. Granfors and R. Aufrichtig, "Performance of a 41×41 cm^2 amorphous silicon flat panel x-ray detector for radiographic imaging applications," Med. Phys. **27**, 1324–1331 (2000).
[35]J. A. Rowlands and W. G. Ji, "Effect of depth dependent modulation transfer function and K-fluorescence re-absorption on the detective quantum efficiency of indirect conversion flat panel x-ray imaging systems using CsI," Proc. SPIE **4320**, 257–267 (2001).
[36]K.-W. Jee, L. E. Antonuk, Y. El-Mohri, and Q. Zhao, "System performance of a prototype flat-panel imager operated under mammographic conditions," Med. Phys. **30**, 1874–1890 (2003).

[37]W. Zhao, G. Ristic, and J. A. Rowlands, "X-ray imaging performance of structured cesium iodide scintillators," Med. Phys. **31**, 2594–2605 (2004).
[38]R. A. Street, J. T. Rahn, S. E. Ready, K. S. Shah, P. R. Bennett, Y. N. Dmitriyev, P. Mei, J. Lu, R. B. Apte, J. Ho, K. Van Schuylenbergh, F. Lemmi, J. B. Boyce, and P. Nylen, "X-ray imaging using lead iodide as a semiconductor detector," Proc. SPIE **3659**, 36–47 (1999).
[39]R. A. Street *et al.*, "High resolution, direct detection x-ray imagers," Proc. SPIE **3977**, 418–428 (2000).
[40]R. A. Street *et al.*, "Comparative study of PbI_2 and HgI_2 as direct detector materials for high resolution x-ray image sensors," Proc. SPIE **4320**, 1–12 (2001).
[41]R. A. Street, S. E. Ready, K. Van Schuylenbergh, J. Ho, J. B. Boyce, P. Nylen, K. Shah, L. Melekhov, and H. Hermon, "Comparison of PbI_2 and HgI_2 for direct detection active matrix x-ray image sensors," J. Appl. Phys. **91**, 3345–3355 (2002).
[42]D. M. Tucker, G. T. Barnes, and D. P. Chakraborty, "Semiempirical model for generating tungsten target x-ray spectra," Med. Phys. **18**, 211–218 (1991).
[43]R. K. Swank, "Calculation of modulation transfer functions of x-ray fluorescent screens," Appl. Opt. **12**, 1865–1870 (1973).
[44]A. Badano and R. Leimbach, "Depth-dependent phosphor blur in indirect x-ray imaging sensors," Proc. SPIE **4682**, 94–106 (2002).
[45]A. Badano, "Optical blur and collection efficiency in columnar phosphors for x-ray imaging," Nucl. Instrum. Methods Phys. Res. A **508**, 467–479 (2003).
[46]G. Hajdok and I. A. Cunningham, "Penalty on the detective quantum efficiency from off-axis incident x rays," Proc. SPIE **5368**, 109–118 (2004).
[47]J. G. Mainprize, A. K. Bloomquist, M. P. Kempston, and M. J. Yaffe, "Resolution at oblique incidence angles of a flat-panel imager for breast tomosynthesis," Med. Phys. **33**, 3159–3164 (2006).
[48]A. Badano, I. S. Kyprianou, and J. Sempau, "Anisotropic imaging performance in indirect x-ray imaging detectors," Med. Phys. **33**, 2698–2713 (2006).
[49]A. Badano, I. S. Kyprianou, R. J. Jennings, and J. Sempau, "Anisotropic imaging performance in breast tomosynthesis," Med. Phys. **34**, 4076–4091 (2007).
[50]A. Sawant, L. E. Antonuk, Y. El-Mohri, Y. Li, Z. Su, Y. Wang, J. Yamamoto, Q. Zhao, and H. Du, "Segmented phosphors: MEMS-based high quantum efficiency detectors for megavoltage x-ray imaging," Med. Phys. **32**, 553–565 (2005).
[51]A. Sawant, L. E. Antonuk, Y. El-Mohri, Q. Zhao, Y. Li, Z. Su, Y. Wang, J. Yamamoto, H. Du, I. Cunningham, M. Klugerman, and K. Shah, "Segmented crystalline scintillators: An initial investigation of high quantum efficiency detectors for megavoltage x-ray imaging," Med. Phys. **32**, 3067–3083 (2005).
[52]A. Sawant, L. E. Antonuk, Y. El-Mohri, Q. Zhao, Y. Wang, Y. Li, and H. Du, "Segmented crystalline scintillators: Empirical and theoretical investigation of a high-quantum efficiency EPID based on an initial engineering prototype CsI(Tl) detector," Med. Phys. **33**, 1053–1066 (2006).
[53]W. Zhao, W. G. Ji, and J. A. Rowlands, "Effects of characteristic x rays on the noise power spectra and detective quantum efficiency of photoconductive x-ray detectors," Med. Phys. **28**, 2039–2049 (2001).
[54]G. Hajdok, J. J. Battista, and I. A. Cunningham, "Fundamental x-ray interaction limits in diagnostic imaging detectors: Frequency-dependent Swank noise," Med. Phys. **35**, 3194–3204 (2008).